MATERIALS CHEMISTRY FRONTIERS

RESEARCH ARTICLE

View Article Online
View Journal

Cite this: DOI: 10.1039/d6qm00236f

Strain regulation for phase-pure and stable wide-bandgap $FAPbBr_3$ perovskite solar cells

Hasnain Raza,†[ab] Zijin Qiao,†[ac] Huanyi Zhou,[a] Jiayu Zheng,[ac] Hui-Ming Cheng[a] and Zaiwei Wang *[a]

Received 30th March 2026,
Accepted 9th April 2026

DOI: 10.1039/d6qm00236f

rsc.li/frontiers-materials

Wide-bandgap lead bromide perovskites are ideal candidates for perovskite solar cells (PSCs) requiring high open-circuit voltages (V_{OC}), particularly as front absorbers in multiple-junction architectures. However, the formation of a photoinactive non-perovskite δ-phase (δ-$FAPbBr_3$) is a critical issue that inhibits the photovoltaic performance of the devices. In this work, we introduce sodium 4-chlorobenzenesulfonate (4Cl-BZS) to inhibit the formation of the δ-phase and release lattice strain, thus preparing perovskite thin films with a pure phase. Consequently, inverted $FAPbBr_3$ solar cells achieve a champion power conversion efficiency (PCE) of 10.57% and a high V_{OC} of 1.63 V, representing one of the best performances for this configuration. Furthermore, unencapsulated devices retain over 90% of their initial efficiency after 1400 h of aging under 50% relative humidity, demonstrating excellent environmental stability.

Introduction

Hybrid organic–inorganic metal halide perovskite solar cells (PSCs) have become one of the most promising photovoltaic technologies with the record breaking gains in power conversion efficiency that has already reached around 27% in a short period.[1–5] Composition changes can alter the optical and physical properties of lead halide perovskites with the general ABX_3 structure,[6–8] where the A site is usually occupied by a monovalent cation, usually methylammonium (MA^+),[9,10] cesium (Cs^+),[11–14] or formamidinium (FA^+),[15,16] whereas the B site is occupied by a divalent metal cation (typically Pb^{2+} or Sn^{2+}),[17] and the X site is occupied by a halide anion (Br^- or I^-).[18] A relatively easy method of changing the bandgap is to change the halide component. For instance, replacing iodide with bromide leads to a wider band gap. Bromide-based wide-bandgap perovskites exhibit high V_{OC} and superior chemical, phase, and humidity stability compared to their iodide-based counterparts, rendering them ideal wide-bandgap top absorbers for multiple-junction solar cells.[15,16,19–21] These bromide based wide band-gap perovskites are most notably useful in perovskite based multiple-junction solar cells.[19] These architectures are critical for transcending the Shockley–Queisser efficiency limit (~33%) of single-junction devices by efficiently harvesting high-energy photons.[20]

$FAPbBr_3$ is particularly promising among wide-bandgap (~2.3 eV) absorbers.[21–23] Various strategies have been explored in the recent past in order to improve the performance of $FAPbBr_3$ perovskite solar cells. For example, Xu *et al.* proposed the use of guanidinium bromide (GABr) to control the crystallization process and to minimize the density of defects in $FAPbBr_3$ films, which led to improved film quality and device performance.[24] The surface passivation technique was reported to reduce nonradiative recombination and have an effect on the stability of the $FAPbBr_3$ devices.[25] Additionally, Zhu *et al.* reported a carbazole based self-assembled monolayer at the hole selective interface to improve energy level alignment and charge extraction in $FAPbBr_3$ devices.[26]

Despite these efforts, $FAPbBr_3$ films suffer from a persistent issue: the spontaneous formation of the δ-phase.[24] The photoactive α-phase consists of a three-dimensional corner-sharing $[PbBr_6]^{4-}$ octahedral network, whereas the thermodynamically stable δ-phase adopts a non-perovskite, edge-sharing hexagonal structure. This phase impurity severely degrades film crystallinity and introduces non-radiative recombination centers.[27,28] Recent research reveals that accumulated lattice strain destabilizes the photoactive structure, directly inducing the transition to the undesirable δ-phase.[29–31] Therefore, stress management is crucial for fabricating phase-pure and stable $FAPbBr_3$ films.

In this study, we unveil that the incorporation of 4Cl-BZS effectively mitigates residual tensile strain throughout the film depth. Besides, the 4Cl-BZS additive is verified to chemically anchor onto the perovskite surface through strong coordination interactions of its sulfonate and chlorine functional groups with

[a] *Shenzhen Key Laboratory of Energy Materials for Carbon Neutrality, Institute of Technology for Carbon Neutrality, Shenzhen Institutes of Advanced Technology, Chinese Academy of Sciences, Shenzhen, 518055, P. R. China. E-mail: zw.wang3@siat.ac.cn*
[b] *University of Chinese Academy of Sciences, Beijing, 100049, P. R. China*
[c] *Southern University of Science and Technology, Shenzhen, 518055, P. R. China*
† These authors contributed equally.

undercoordinated Pb^{2+}, effectively passivating surface defects. The incorporation of 4Cl-BZS also enlarges the perovskite grain size and plays a pivotal role in facilitating efficient carrier transport while suppressing non-radiative recombination. Consequently, p–i–n based phase pure $FAPbBr_3$ devices using 1 mg mL^{-1} of 4Cl-BZS were successfully fabricated with a champion efficiency of 10.57% and a V_{OC} of 1.63 V. In addition, the 4Cl-BZS modified devices maintained 90% of their initial efficiency after 1400 hours of ambient storage, suggesting good long-term stability.

Results and discussion

Sodium 4-chlorobenzenesulfonate (4Cl-BZS) was directly added to the $FAPbBr_3$ perovskite precursor solution prior to film deposition. X-ray diffraction (XRD) was used to study the effect of the additive on the phase formation of $FAPbBr_3$ perovskite films. Fig. 1a demonstrates that the control and 4Cl-BZS treated films have the typical diffraction peaks of the photoactive α-phase at about 15.0° and 30.0° (2θ), corresponding to the (001) and (002) planes.[27,28,32] Conversely, the control film exhibits a broad diffraction peak at ~12.5° (2θ) that is generally attributed to the non-perovskite δ-phase, not $PbBr_2$ (Fig. S1).[33,34] Besides, this characteristic is highly repressed in the 4Cl-BZS treated film, which means that the additive prevents the formation of the δ-phase during crystallization and promotes the stabilization of the α-phase. Moreover, the 4Cl-BZS treated film has a higher diffraction intensity and lower peak broadening, which indicates a better crystalline coherence. No other diffraction peaks related to the secondary phases or crystalline additive species are detected, which means that 4Cl-BZS does not enter the bulk lattice but affects the crystallization of the perovskite film. The inhibition by the introduction of 4Cl-BZS of the δ-phase formation in $FAPbBr_3$ films can be explained by a strain controlled crystallization process.[35] To further validate the structural and chemical specificities of 4Cl-BZS, control experiments using sodium benzenesulfonate (BZS) and sodium 4-chlorobenzoate (4Cl-BZA) were performed (Fig. S2). BZS only partially suppresses the δ-phase, indicating that the lack of the *para*-chlorine atom results in a molecular length that fails to precisely match the Pb–Pb lattice distance, leading to incomplete strain relaxation. The films treated with 4Cl-BZA still exhibit a severe formation of the photoinactive δ-phase, similar to the untreated control films. These all demonstrate the necessity of the strong coordination environment provided by the sulfonate group and Cl.

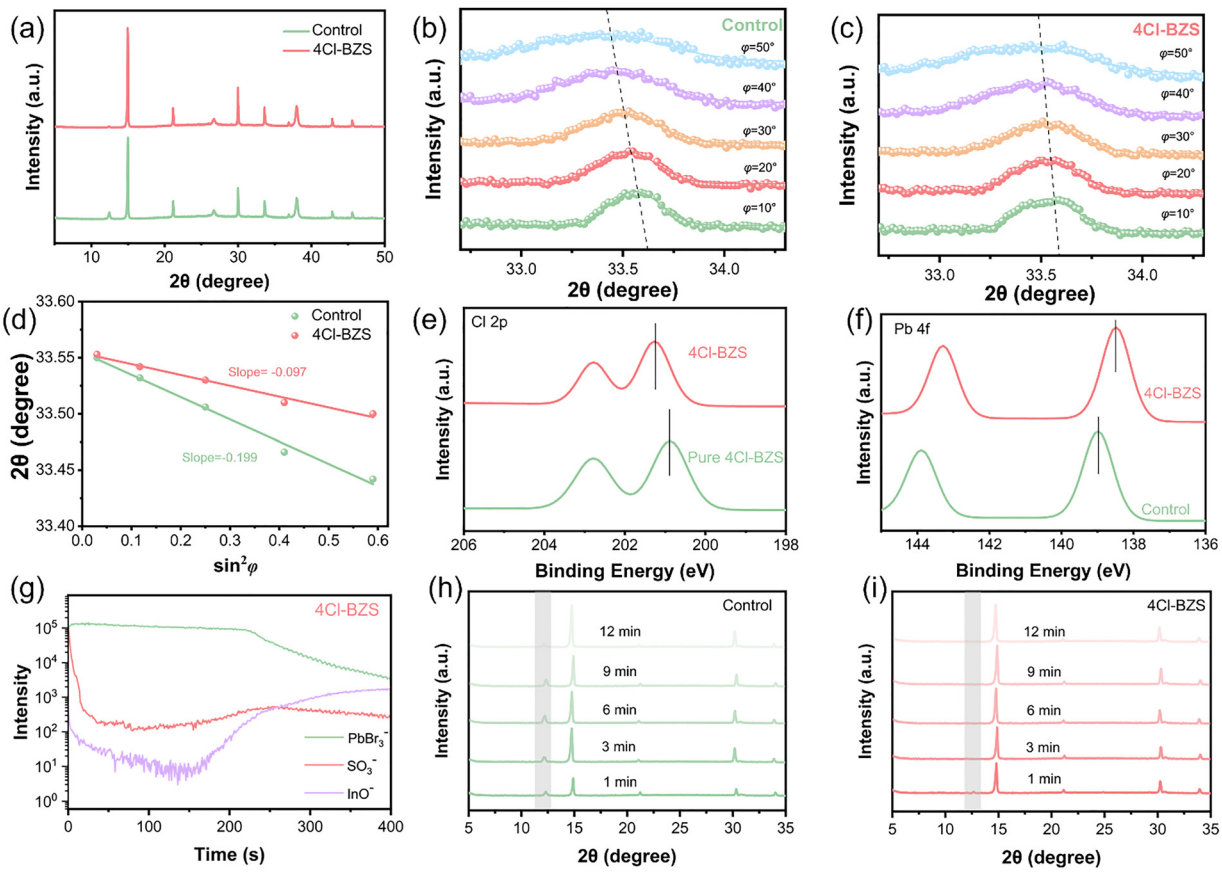

Fig. 1 (a) XRD patterns of the control and 4Cl-BZS modified $FAPbBr_3$ films; (b) and (c) GIXRD patterns with different instrumental ψ values of control and 4Cl-BZS perovskite films; (d) linear fit of 2θ–$\sin^2\psi$ for control and 4Cl-BZS perovskite films; (e) high-resolution Pb 4f XPS spectra of the control and 4Cl-BZS modified films; (f) high-resolution Cl 2p XPS spectra of pure 4Cl-BZS and 4Cl-BZS modified $FAPbBr_3$ films; (g) TOF-SIMS results of the perovskite film with 4Cl-BZS; (h) and (i) XRD patterns of the control and 4Cl-BZS treated perovskite film at different annealing times.

In FA based perovskites, the corner sharing perovskite structure is destabilized by residual lattice strain during film growth, which promotes the formation of a non-perovskite δ-phase structure.[29,36,37] Specifically, 4Cl-BZS has a molecular length of ~6.37 Å, which perfectly matches the distance between two adjacent Pb^{2+} ions (~6.3 Å) in the perovskite lattice.[38] Driven by this dimensional matching, 4Cl-BZS in the crystallization is expected to assist in alleviating the lattice strain of the perovskite phase that ultimately inhibits the formation of the δ-phase and stabilizes the photoactive perovskite structure.[29–31] To further validate the mechanism of strain-induced phase stabilization and quantitatively evaluate the residual stress, we performed X-ray diffraction measurements at various sample tilt angles (ψ). Fig. 1b and c show the corresponding XRD peak evolutions for the control and 4Cl-BZS-treated $FAPbBr_3$ films, respectively. As the ψ increases from 10° to 50°, the diffraction peak of the control film shifts noticeably toward lower angles, indicating the presence of substantial tensile strain. In contrast, the 4Cl-BZS-treated film exhibits a much weaker dependence of the peak position on the tilt angle. The slope of the 2θ–$\sin^2\psi$ fitting curve served as an estimation of the residual stress release in the perovskite film. As shown in Fig. 1d, the extracted slope for the control film is −0.199, and the 4Cl-BZS-treated film displays a significantly reduced slope to −0.097. According to the equation: $\delta_R = -\left(\frac{E}{1+v}\right)_{\{hkl\}} \frac{\Pi}{180}\cot\theta \frac{\partial(2\theta)}{\partial \sin 2\psi}$,[39] where δ_R is the residual stress, E is the Young's modulus of perovskites (11.5 GPa), ν is the Poisson's ratio (0.33), and θ_0 is half of the scattering angle $2\theta_0$ for stress-free perovskite, the tensile stress values of the control perovskite film and the 4Cl-BZS treated film are calculated to be 51.0 and 24.8 MPa, respectively. This pronounced reduction in residual tensile stress provides evidence that the 4Cl-BZS additive effectively alleviates the lattice strain accumulated during crystallization, which consequently suppresses the strain-induced phase transformation to the undesired δ-phase and stabilizes the photoactive structure.[36,40] These observations suggest that the presence of 4Cl-BZS affects the crystallization process, which results in a more homogeneous lattice structure, and offer structural evidence of the proposed mechanism that explains the improved phase stability of the additive treated films. To further quantify the magnitude of the residual strain, a Williamson–Hall (W–H) analysis based on the standard XRD patterns is shown in Fig. S3. The W–H equation is given by $\beta_{hkl}\cos\theta = \frac{K\lambda}{D} + 4\varepsilon\sin\theta$. β_{hkl} is the full width at half maximum (FWHM) of the diffraction peak, θ is the Bragg angle, K is the shape factor, λ is the X-ray wavelength, D is the crystallite size, and ε is the strain factor.[41] As shown in Fig. S3, the extracted microstrain (ε) of the 4Cl-BZS treated film is significantly reduced to 1.16×10^{-3}, compared to 4.32×10^{-3} for the control film. This quantitative reduction firmly substantiates that 4Cl-BZS effectively alleviates the tensile microstrain within the perovskite lattice.

X-ray photoelectron spectroscopy (XPS) was used to examine the chemical environment of $FAPbBr_3$ films on the surface and to examine the interaction between the perovskite and the 4Cl-BZS additive. The high resolution Pb 4f spectra of the control and 4Cl-BZS treated films are presented in Fig. 1b. The two samples have the typical Pb $4f_{7/2}$ and Pb $4f_{5/2}$ doublet that is related to Pb^{2+}. The Pb 4f peaks of 4Cl-BZS treated films exhibit a shift towards a lower binding energy of approximately 0.2 eV than the control film, indicating effective passivation of under-coordinated Pb sites.[42] The interaction between the Cl and Pb on the 4Cl-BZS additive perovskite surface is also confirmed by the Cl 2p XPS spectrum (Fig. 1c), where the Cl 2p peak of the treated film has a slight shift to higher binding energy than that of the pristine 4Cl-BZS. To further corroborate this interaction mechanism, Fourier transform infrared (FTIR) spectroscopy was conducted (Fig. S4). The characteristic S=O stretching vibrations of 4Cl-BZS at 1349 and 1189 cm^{-1} exhibit distinct blue shifts to 1355 and 1193 cm^{-1} upon mixing with $PbBr_2$, confirming the formation of a strong coordination bond between the sulfonate oxygen and Pb^{2+}. Thermogravimetric analysis (TGA) and differential scanning calorimetry (DSC) measurements were further performed to examine the thermal stability of 4Cl-BZS. As shown in Fig. S5, no obvious decomposition occurs below the annealing temperature used for perovskite film formation, indicating that 4Cl-BZS remains stable during the annealing process.

To ascertain the precise spatial distribution of 4Cl-BZS and further elucidate the strain regulation mechanism, Time-of-Flight Secondary Ion Mass Spectrometry (TOF-SIMS) depth profiling was conducted, as shown in Fig. 1g. The characteristic ion signals SO_3^- associated with 4Cl-BZS showed that the 4Cl-BZS molecules are highly concentrated near the top surface of the $FAPbBr_3$ perovskite film, rather than being uniformly distributed in the bulk. During the spin-coating and crystallization process, the top surface undergoes rapid solvent evaporation, making it highly susceptible to the accumulation of severe residual tensile strain. By enriching at this critical upper interface, 4Cl-BZS specifically targets and alleviates the localized tensile strain. Moreover, the *ex situ* time-dependent XRD patterns were used to investigate the process of tensile strain alleviation. As shown in Fig. 1h, the control film exhibits a prominent diffraction peak at ~12.5° corresponding to the photoinactive δ-phase immediately upon annealing. This phase impurity persists throughout the entire 12-minute heating process, indicating that the rapid, uncontrolled crystallization kinetically traps the lattice in the undesirable non-perovskite structure. In contrast, the 4Cl-BZS treated film (Fig. 1i) displays a fundamentally different phase evolution. While a trace amount of the δ-phase is initially observed at the 1-minute mark, it is rapidly and completely consumed by the 3-minute mark, yielding a highly crystalline, pure α-phase that remains exceptionally stable thereafter. It is highly plausible that the coordination between 4Cl-BZS and Pb^{2+} acts as an intermediate-phase regulator during the early heating stage, facilitating the swift structural transition from the δ-phase to the desired corner-sharing α-phase. Ultimately, this modulated crystallization process helps to prevent the accumulation of lattice strain, ensuring a phase-pure perovskite film.

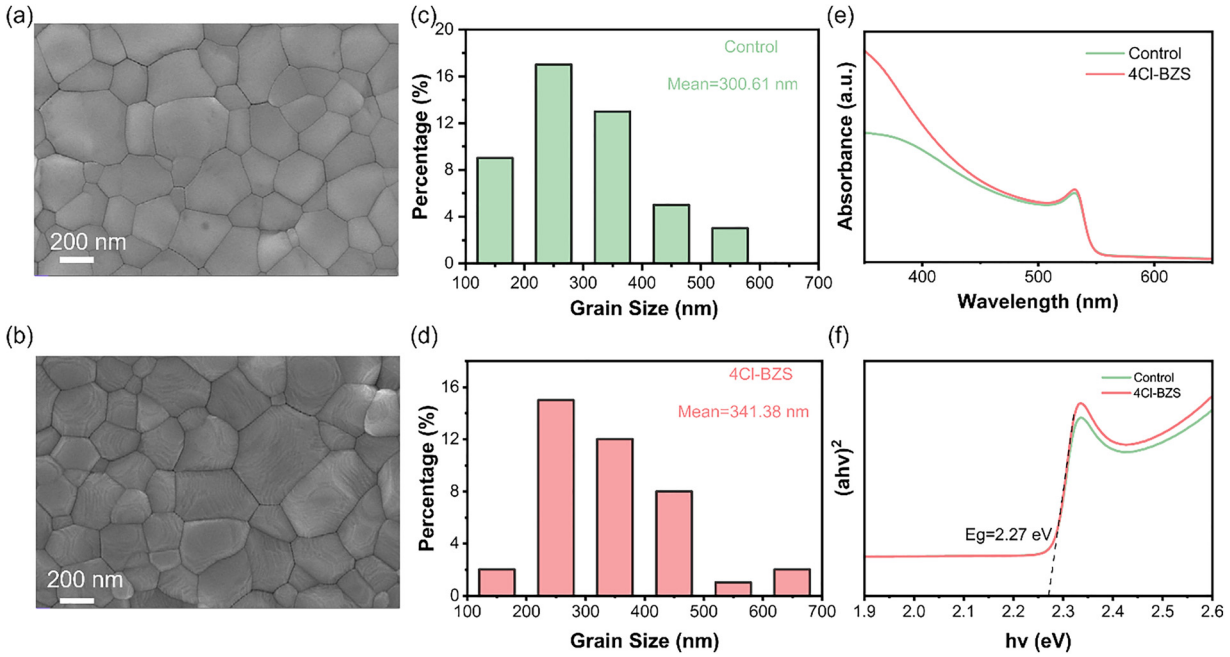

Fig. 2 (a) and (b) Top view SEM images of the control and 4Cl-BZS-modified $FAPbBr_3$ films; (c) and (d) histograms of the grain size distributions of the control and 4Cl-BZS modified films; (e) UV-vis absorption spectra of the control and 4Cl-BZS modified films; and (f) Tauc plots of the control and 4Cl-BZS modified films.

The surface morphology of the $FAPbBr_3$ films with and without the 4Cl-BZS additive was observed using top view scanning electron microscopy (SEM), as shown in Fig. 2a and b. The control film is composed of relatively smaller grains, whereas the film treated with 4Cl-BZS has larger grains with clearly defined grain boundaries. Fig. 2c and d summarize grain size distributions obtained using the SEM images. The average grain size of the control film is about 300.6 nm, but the 4Cl-BZS treated film has a higher average grain size of about 341.4 nm. These results suggest that 4Cl-BZS affects the crystallization of $FAPbBr_3$, which results in a greater growth of grains. Specifically, the impact of 4Cl-BZS on spin crystallization dynamics is clearly visualized in the *in situ* PL maps. After dropping the anti-solvent, while the control film (Fig. S6a) undergoes a rapid phase transition evidenced by the sharp rise in PL intensity, the addition of 4Cl-BZS (Fig. S6b) results in a prolonged growth window. The time to reach the peak PL intensity is delayed, and the intensity slope is gentler compared to that of the control. This observation aligns well with the intermediate phase mechanism, where the 4Cl-BZS additive regulates the reaction kinetics, suppressing excessive nucleation and promoting orderly crystal growth.[40] The optical absorption properties of the $FAPbBr_3$ films were analyzed by measuring the UV-vis absorption spectra. Fig. 2e demonstrates that the control and 4Cl-BZS treated films have a similar absorption profile with a distinct absorption edge, which suggests that the films have a similar light harvesting activity. The 4Cl-BZS treated film exhibits slightly increased intensity of absorption in the visible range as compared to control, indicating that the 4Cl-BZS treated films can generate more charge carriers when exposed to the same light intensity. Tauc plots based on the absorption data were also used to further estimate the optical bandgap (Fig. 2f). The optical bandgap in both films is nearly identical (2.27 eV), which proves that the introduction of 4Cl-BZS does not alter the band structure of $FAPbBr_3$.[43]

To assess radiative recombination behavior of $FAPbBr_3$ films, steady state photoluminescence (PL) measurements were carried out, as shown in Fig. 3a. The PL intensity of the 4Cl-BZS treated film is much higher than that of the control film, indicating that non-radiative recombination is effectively suppressed in the presence of the additive.[44] Time-resolved photoluminescence (TRPL) measurements (Fig. 3b) reveal a longer average carrier lifetime of the 4Cl-BZS treated film compared to that of the control film. The prolonged carrier lifetime stems from the improved perovskite film quality induced by 4Cl-BZS, which effectively suppresses non-radiative recombination. The TRPL decay profiles are analyzed using a bi-exponential model of fast and slow decay components, with the extracted average carrier lifetime being higher in the case of the 4Cl-BZS treated film (Table S1).

Space charge limited current (SCLC) measurements were employed to quantify the trap states using electron-only ITO/SnO_x/perovskite (with or without 4Cl-BZS)/PCBM/Ag. The dark current density–voltage (*J–V*) curves (Fig. 3c) exhibit the typical transition from the ohmic to the trap-filled limit (TFL) regime. The trap density (N_{trap}) was calculated using the equation $N_{trap} = \frac{2\varepsilon\varepsilon_0 V_{TFL}}{qL^2}$.[45] Upon the incorporation of 4Cl-BZS, the V_{TFL} decreased from 0.56 V to 0.43 V for electron-only devices. Additionally, the electron trap densities N_t of control and 4Cl-BZS devices are 1.87×10^{16} cm^{-3} and 1.43×10^{16} cm^{-3}, respectively (Table S2). Specifically, the suppression of non-

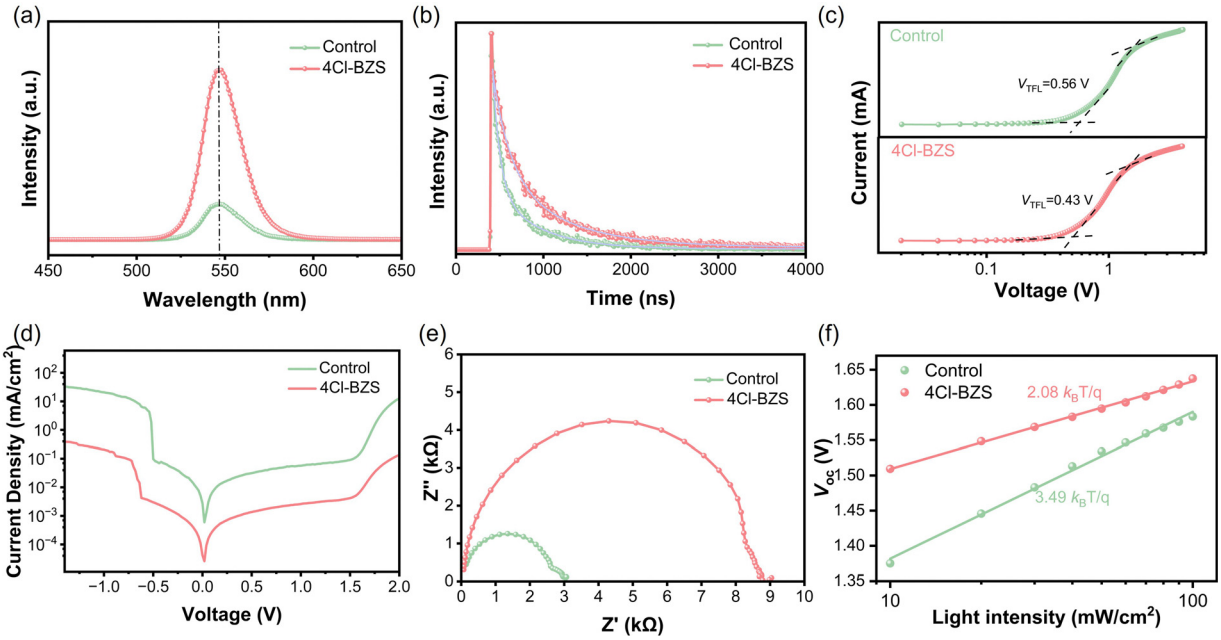

Fig. 3 (a) Steady-state PL spectra and (b) TRPL decays of the perovskite films deposited on ITO; (c) electron only device current density–voltage J–V curves used to analyze space charge limited current (SCLC) of the control and 4Cl-BZS devices; (d) J–V curves of the control and 4Cl-BZS devices; (e) Nyquist plots obtained by electrochemical impedance spectroscopy (EIS) measurements based on the control and 4Cl-BZS devices; and (f) the influence of light intensity on V_{OC} of control and 4Cl-BZS devices.

radiative recombination is a synergistic outcome of strain regulation, improved crystallinity, and chemical passivation. By mitigating the lattice strain gradient and passivating defects by 4Cl-BZS, we fundamentally suppress the formation of trap states, thereby minimizing non-radiative recombination and promoting charge transport. Consequently, Mott–Schottky measurements (Fig. S7) show an increased built-in potential (V_{bi}) from 1.35 V to 1.48 V after 4Cl-BZS treatment, providing a stronger internal electric field to drive charge separation and enhance the V_{OC}.[26]

Furthermore, the reduced dark saturation current density in the 4Cl-BZS device suggests fewer bulk defects within the perovskite layer and suppressed non-radiative recombination (Fig. 3d).[46] These results indicate that the incorporation of 4Cl-BZS effectively mitigates trap-assisted recombination and facilitates charge transport, ultimately contributing to the improved V_{OC} of the modified devices. In order to examine the interfacial charge transfer behavior of the devices, electrochemical impedance spectroscopy (EIS) measurements were conducted under dark conditions, as shown in Fig. 3e. The results indicate that the device containing 4Cl-BZS has a higher recombination resistance (R_{rec}) than the control device. The improvement in R_{rec} with the 4Cl-BZS device is in line with the reduction in trap states, lower charge recombination and better carrier extraction. The recombination characteristics of the devices were also examined by evaluating how open-circuit voltage (V_{OC}) varies with the light intensity (Fig. 3f). The fitting slope of the 4Cl-BZS film is lower compared with that of the control device, 3.49 to $2.08kT/q$ (where k is the Boltzmann constant, T is the temperature and q is the elementary charge). The lower slope is an indicator of repressed trap assisted recombination in the 4Cl-BZS modified device, which implies that the recombination kinetics are more favorable because of the enhanced defect passivation in the perovskite film.[47]

We fabricated p–i–n PSCs with a structure of ITO/NiO_x/SAM/$FAPbBr_3$(4Cl-BZS)/PCBM/SnO_x/Ag(Fig. 4a); the cross-view SEM images of the device with 4Cl-BZS are shown in Fig. S8. Through device optimization, the concentration of 4Cl-BZS was determined to be 1 mg mL^{-1} (Fig. S9) to achieve the best efficiency. Fig. 4b shows the comparison between the J–V characteristics of the control and the best concentration of 4Cl-BZS treated $FAPbBr_3$ perovskite solar cells under optimized conditions with the photovoltaic parameters. The 4Cl-BZS treated device provides a power conversion efficiency (PCE) of up to 10.57%, along with a V_{OC} of 1.63 V, a short circuit current density (J_{SC}) of 7.76 mA cm^{-2} and a high fill factor (FF) of 83.73%. As illustrated in Fig. S10, 4Cl-BZS effectively minimized the hysteresis behavior of the devices. The calculated hysteresis factor $\left(\mathrm{HF} = \frac{\mathrm{PCE_{Reverse}} - \mathrm{PCE_{Forward}}}{\mathrm{PCE_{Reverse}}}\right)$ decreased from 3.23% for the control to 1.99% for the 4Cl-BZS treated device. This suppression of hysteresis is a direct macroscopic reflection of the improved structural robustness. This reduced hysteresis is mainly due to the improved structural stability of the $FAPbBr_3$ film. By effectively suppressing the yellow phase and relieving the internal strain, 4Cl-BZS makes the perovskite crystal lattice more stable. As a result, ion migration is largely restricted, leading to minimized hysteresis. External quantum efficiency (EQE) spectra of two devices are shown in Fig. 4c. The higher integrated short circuit current density of the 4Cl-BZS

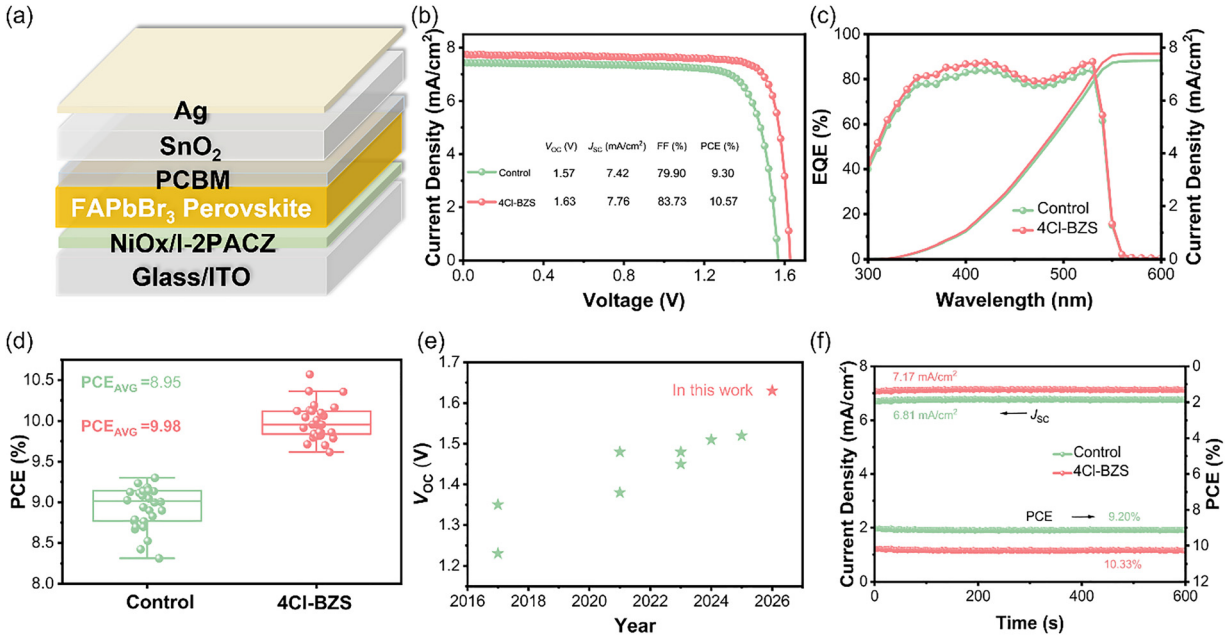

Fig. 4 (a) Schematic representation of the p–i–n device architecture. (b) AM 1.5G illuminated *J*–*V* curves. (c) EQE spectra along with the cumulative current densities. (d) Statistical distribution of the power conversion efficiency (PCE) of control and 4Cl-BZS devices.[26,27,48–53] (e) Comparison of the open-circuit voltage (V_{OC}) obtained in this study with that of the devices reported before on the basis of $FAPbBr_3$. (f) Stabilized power output (SPO) at the operating point.

treated device is in line with the improved light to current conversion in the *J*–*V* characteristics. Statistical analysis of data from 30 individual devices reveals that upon the incorporation of 4Cl-BZS, the average PCE increased from 8.95% to 9.98%, accompanied by significant improvements in V_{OC}, J_{SC} and FF (Fig. 4e and Fig. S11).

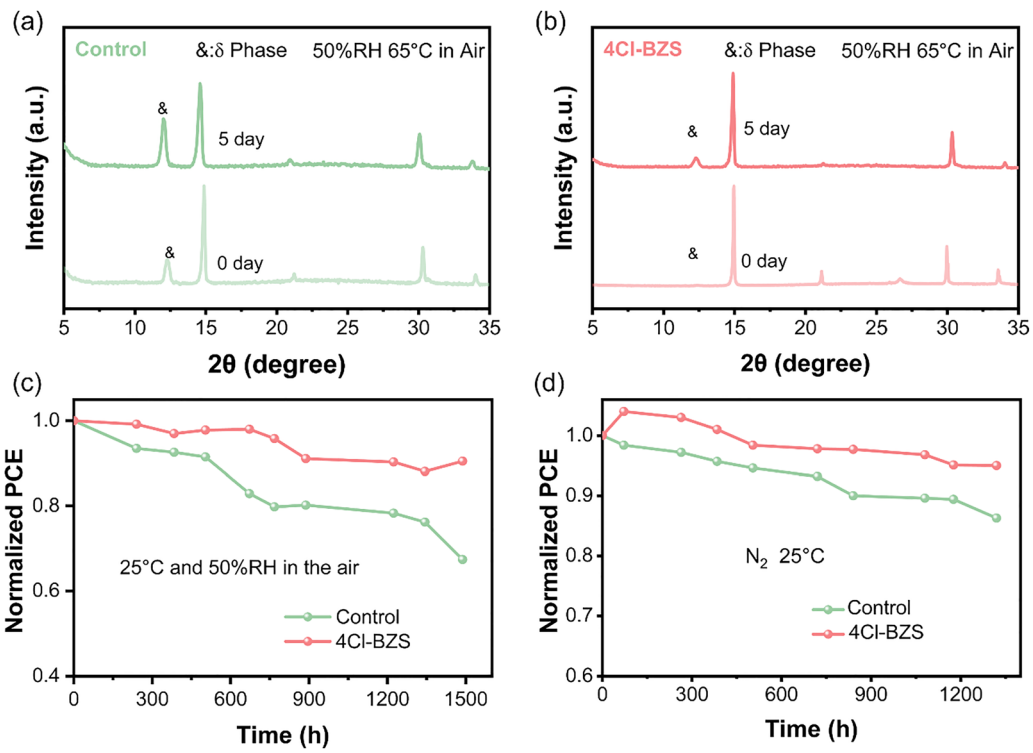

Fig. 5 (a) and (b) XRD stability curves of control and 4Cl-BZS modified films. (c) Evolution of unencapsulated devices in ambient air at around 25 °C and 50% relative humidity at the normalized PCE. (d) PCE evolution of unencapsulated devices in a nitrogen atmosphere at 25 °C.

Fig. 4f and Table S3 compare the V_{OC} obtained in this work to previously reported values of $FAPbBr_3$ perovskite solar cells, indicating that the current device performance is among the higher values reported. Fig. 4c demonstrates the steady state power output (SPO) of the control and 4Cl-BZS treated devices at the maximum power point (MPP) over 600 s. The 4Cl-BZS treated film has a stabilized current density of 7.17 mA cm^{-2}, which is greater than that of the control device (6.81 mA cm^{-2}). Also, the treated and control devices are found to have stabilized power conversion efficiencies of 10.33% and 9.20%, respectively, which suggests that the operational stability of the devices improves when 4Cl-BZS is incorporated.

Given that 4Cl-BZS effectively inhibits the formation of the δ-phase, we further investigated its impact on the long-term stability of both the thin films and the corresponding devices. Fig. 5a and b compare the XRD patterns of $FAPbBr_3$ films after 5 days of aging. The control film exhibits a prominent peak corresponding to the δ-phase, indicating significant degradation. In contrast, the 4Cl-BZS treated film suppresses δ-phase formation and retains the crystallinity of the photoactive α-phase, demonstrating superior phase stability. Meanwhile, Fig. 5c illustrates the long-term storage stability of unencapsulated devices under ambient conditions (25 °C, approximately 50% relative humidity). The control device shows a continuous efficiency degradation during aging, which loses over 40% of its original PCE in 1500 h. The 4Cl-BZS treated devices, however, exhibit a significantly slower degradation rate and retain 90% of their original efficiency after the same time. In addition, after 1300 h of storage in an inert N_2 atmosphere at 25 °C, the 4Cl-BZS treated device retains nearly 95% of its original efficiency after aging of approximately 1300 h, whereas the control device is able to retain over 80% (Fig. 5d). Fundamentally, the superior long-term stability of the 4Cl-BZS-treated devices is governed by enhanced phase thermodynamics. The effective relief of residual tensile strain inherently eliminates the thermodynamic driving force for the spontaneous α–δ phase transition, thereby preventing the formation of the photoinactive yellow phase. Furthermore, the strong chemical anchoring of 4Cl-BZS at the surfaces and grain boundaries acts as a robust molecular shield, contributing to the excellent moisture tolerance observed during ambient aging.

Conclusions

Overall, this study demonstrates that the residual strain can be controlled as an effective method to inhibit the formation of the photoinactive δ phase and stabilize the photoactive δ phase in wide bandgap $FAPbBr_3$ perovskites. The 4Cl-BZS during the film formation inhibits the accumulation of strain and prevents the strain induced formation of non-perovskite structures, thus promoting the formation of a stable, corner sharing perovskite lattice. Consequently, inverted p–i–n $FAPbBr_3$ solar cells have been reported to show a power conversion efficiency of 10.57% and a V_{OC} of 1.63 V, placing this work among the higher-performing reports for this material system. In addition, the treated devices remain highly stable over time, retaining more than 90% of their initial efficiency after extended aging in both humid air and inert environments.

Author contributions

H. R. and Z. W. conceived the research. H. R. and Z. J. designed the experiments, analyzed the data, and wrote the manuscript. H. R. and Z. J. fabricated the perovskite devices and characterized the devices. H. M. and Z. W. directed and supervised the project and revised this manuscript. H. Y. and J. Y. assisted with characterization. All authors discussed the results and contributed to revising the manuscript.

Conflicts of interest

The authors declare that they have no conflicts of interest.

Data availability

All data generated or analyzed during this study are included in the published article and its supplementary information (SI). See DOI: **https://doi.org/10.1039/d6qm00236f**.

Additional data are available from the corresponding author upon request.

Acknowledgements

This work was supported by the Shenzhen Science and Technology Program (JCYJ20241202124937050).

References

1 S. Li, Y. Jiang, J. Xu, D. Wang, Z. Ding, T. Zhu, B. Chen, Y. Yang, M. Wei, R. Guo, Y. Hou, Y. Chen, C. Sun, K. Wei, S. M. H. Qaid, H. Lu, H. Tan, D. Di, J. Chen, M. Grätzel, E. H. Sargent and M. Yuan, High-efficiency and thermally stable $FACsPbI_3$ perovskite photovoltaics, *Nature*, 2024, **635**, 82–88.

2 Y. Shi, X. Cheng, Y. Wang, W. Li, W. Shang, W. Liu, W. Lu, J. Cheng, L. Liu and Y. Shi, Atomically Dispersed Metal Atoms: Minimizing Interfacial Charge Transport Barrier for Efficient Carbon-Based Perovskite Solar Cells, *Nano-Micro Lett.*, 2025, **17**, 125.

3 Y. Li, Z. Zheng, X. Zheng, X. Liu, Y. Yang, Y. Zhu, Z. Wang, X. Ren, M. Fu, R. Guo, J. Guo, Z. Xiao, Y. Rong and X. Li, Mutual stabilization of hybrid and inorganic perovskites for photovoltaics, *eScience*, 2026, **6**, 100449.

4 G. Li, Z. Zhang, B. Agyei-Tuffour, L. Wu, T. W. Gries, K. Prashanthan, L. Frohloff, A. Musiienko, J. Li, R. Zhu, L. J. F. Hart, L. Wang, Z. Li, B. Hou, N. Koch, M. Saba, P. R. F. Barnes, J. Nelson, P. J. Dyson, M. K. Nazeeruddin, M. Li and A. Abate, Stabilizing high-efficiency perovskite solar cells via strategic interfacial contact engineering, *Nat. Photon.*, 2026, **20**, 55–62.

5 W. Wu, H. Gao, L. Jia, Y. Li, D. Zhang, H. Zhan, J. Xu, B. Li, Z. Geng, Y. Cheng, H. Tong, Y. Pan, J. Liu, Y. He, X. Xu, Z. Li, B. He, M. Zhou, L. Wang and C. Qin, Stable and uniform self-assembled organic diradical molecules for perovskite photovoltaics, *Science*, 2025, **389**, 195–199.
6 X. Zhang, Z. Cao, L. Shen, K. Garden, N. Chakraborty, P. Baral, L. Whittaker-Brooks, X. Gong, J. M. Luther and H. Wang, Unraveling the Combined Photothermal Stability of Common Perovskite Solar Cell Compositions, *ACS Energy Lett.*, 2024, **9**, 5728–5736.
7 C. Yi, J. Luo, S. Meloni, A. Boziki, N. Ashari-Astani, C. Grätzel, S. M. Zakeeruddin, U. Röthlisberger and M. Grätzel, Entropic stabilization of mixed A-cation ABX_3 metal halide perovskites for high performance perovskite solar cells, *Energy Environ. Sci.*, 2016, **9**, 656–662.
8 T. Jesper Jacobsson, J.-P. Correa-Baena, M. Pazoki, M. Saliba, K. Schenk, M. Grätzel and A. Hagfeldt, Exploration of the compositional space for mixed lead halogen perovskites for high efficiency solar cells, *Energy Environ. Sci.*, 2016, **9**, 1706–1724.
9 J. Huang, S. Xiang, J. Yu and C.-Z. Li, Highly efficient prismatic perovskite solar cells, *Energy Environ. Sci.*, 2019, **12**, 929–937.
10 X. Hu, X. Jiang, X. Xing, L. Nian, X. Liu, R. Huang, K. Wang, H. Yip and G. Zhou, Wide-bandgap perovskite solar cells with large open-circuit voltage of 1653 mV through interfacial engineering, *Solar RRL*, 2018, **2**, 1800083.
11 Y. Zhao, J. Zhu, B. He and Q. Tang, Dimensionality control of SnO_2 films for hysteresis-free, all-inorganic $CsPbBr_3$ perovskite solar cells with efficiency exceeding 10%, *ACS Appl. Mater. Interfaces*, 2021, **13**, 11058–11066.
12 Y. Haruta, T. Ikenoue, M. Miyake and T. Hirato, One-step coating of full-coverage CsPbBr3 thin films via mist deposition for all-inorganic perovskite solar cells, *ACS Appl. Energy Mater.*, 2020, **3**, 11523–11528.
13 Y. Xu, J. Duan, X. Yang, J. Du, Y. Wang, Y. Duan and Q. Tang, Lattice-tailored low-temperature processed electron transporting materials boost the open-circuit voltage of planar $CsPbBr_3$ perovskite solar cells up to 1.654 V, *J. Mater. Chem. A*, 2020, **8**, 11859–11866.
14 C. Chen, X. Lu, X. Hu, G. Liang and G. Fang, Solution fabrication methods and optimization strategies of $CsPbBr_3$ perovskite solar cells, *J. Mater. Chem. C*, 2024, **12**, 16–28.
15 F. Jafarzadeh, L. A. Castriotta, M. Legrand, D. Ory, S. Cacovich, Z. Skafi, J. Barichello, F. De Rossi, F. Di Giacomo, A. Di Carlo, T. Brown, F. Brunetti and F. Matteocci, Flexible, transparent, and bifacial perovskite solar cells and modules using the wide-band gap $FAPbBr_3$ perovskite absorber, *ACS Appl. Mater. Interfaces*, 2024, **16**, 17607–17616.
16 W. Yue, H. Yang, H. Cai, Y. Xiong, T. Zhou, Y. Liu, J. Zhao, F. Huang, Y. Cheng and J. Zhong, Printable high-efficiency and stable $FAPbBr_3$ perovskite solar cells for multifunctional building-integrated photovoltaics, *Adv. Mater.*, 2023, **35**, 2301548.
17 W. Zhang, H. Yuan, X. Li, X. Guo, C. Lu, A. Liu, H. Yang, L. Xu, X. Shi, Z. Fang, H. Yang, Y. Cheng and J. Fang, Component distribution regulation in Sn-Pb perovskite solar cells through selective molecular interaction, *Adv. Mater.*, 2023, **35**, 2303674.
18 R. Roy, M. M. Byranvand, M. R. Zohdi, T. Magorian Friedlmeier, C. Das, W. Hempel, W. Zuo, M. Kedia, J. J. Rendon, S. Boehringer, B. Hailegnanw, M. Vorochta, S. Mehl, M. Rai, A. Kulkarni, S. Mathur and M. Saliba, All-inorganic $CsPbI_2Br$ perovskite solar cells with thermal stability at 250 °C and moisture-resilience via polymeric protection layers, *Energy Environ. Sci.*, 2025, **18**, 1920–1928.
19 Y. Son, J. Lim, A. K. Le, B.-S. Kim, S. Song and H. Kim, A review of perovskite/Si tandem solar cells: internal and external components toward high efficiency, long-term durability, and commercialization, *Mater. Chem. Front.*, 2026, **10**, 21–51.
20 C. Yan, J. Huang, D. Li and G. Li, Recent progress of metal-halide perovskite-based tandem solar cells, *Mater. Chem. Front.*, 2021, **5**, 4538–4564.
21 A. A. Zhumekenov, M. I. Saidaminov, M. A. Haque, E. Alarousu, S. P. Sarmah, B. Murali, I. Dursun, X.-H. Miao, A. L. Abdelhady, T. Wu, O. F. Mohammed and O. M. Bakr, Formamidinium lead halide perovskite crystals with unprecedented long carrier dynamics and diffusion length, *ACS Energy Lett.*, 2016, **1**, 32–37.
22 F. C. Hanusch, E. Wiesenmayer, E. Mankel, A. Binek, P. Angloher, C. Fraunhofer, N. Giesbrecht, J. M. Feckl, W. Jaegermann, D. Johrendt, T. Bein and P. Docampo, Efficient planar heterojunction perovskite solar cells based on formamidinium lead bromide, *J. Phys. Chem. Lett.*, 2014, **5**, 2791–2795.
23 A. F. Akbulatov, L. A. Frolova, N. N. Dremova, I. Zhidkov, V. M. Martynenko, S. A. Tsarev, S. Yu. Luchkin, E. Z. Kurmaev, S. M. Aldoshin, K. J. Stevenson and P. A. Troshin, Light or heat: what is killing lead halide perovskites under solar cell operation conditions?, *J. Phys. Chem. Lett.*, 2020, **11**, 333–339.
24 H. Xu, Z. Liang, J. Ye, S. Xu, Z. Wang, L. Zhu, X. Chen, Z. Xiao, X. Pan and G. Liu, Guanidinium-assisted crystallization modulation and reduction of open-circuit voltage deficit for efficient planar FAPbBr3 perovskite solar cells, *Chem. Eng. J.*, 2022, **437**, 135181.
25 Y. Liu, B. J. Kim, H. Wu, G. Boschloo and E. M. J. Johansson, Efficient and stable $FAPbBr_3$ perovskite solar cells via interface modification by a low-dimensional perovskite layer, *ACS Appl. Energy Mater.*, 2021, **4**, 9276–9282.
26 H. Zhu, Z. Xu, Z. Zhang, S. Lian, Y. Wu, D. Zhang, H. Zhan, L. Wang, L. Han and C. Qin, Improved Hole-Selective Contact Enables Highly Efficient and Stable $FAPbBr_3$ Perovskite Solar Cells and Semitransparent Modules, *Adv. Mater.*, 2024, **36**, 2406872.
27 H. Zhu, W. Wu, Y. Wu, D. Zhang, H. Zhan, Y. Cheng, L. Wang and C. Qin, δ-Phase Management of $FAPbBr_3$ for Semitransparent Solar Cells, *Adv. Opt. Mater.*, 2023, **11**, 2202827.

28 Y. Wang, Y. Wang, T. A. S. Doherty, S. D. Stranks, F. Gao and D. Yang, Octahedral units in halide perovskites, *Nat. Rev. Chem.*, 2025, **9**, 261–277.
29 S. Masi, A. F. Gualdrón-Reyes and I. Mora-Seró, Stabilization of black perovskite phase in $FAPbI_3$ and $CsPbI_3$, *ACS Energy Lett.*, 2020, **5**, 1974–1985.
30 M. Liu, Y. Chen, C.-S. Tan, R. Quintero-Bermudez, A. H. Proppe, R. Munir, H. Tan, O. Voznyy, B. Scheffel, G. Walters, A. P. T. Kam, B. Sun, M.-J. Choi, S. Hoogland, A. Amassian, S. O. Kelley, F. P. García De Arquer and E. H. Sargent, Lattice anchoring stabilizes solution-processed semiconductors, *Nature*, 2019, **570**, 96–101.
31 J.-W. Lee, S. Tan, T.-H. Han, R. Wang, L. Zhang, C. Park, M. Yoon, C. Choi, M. Xu, M. E. Liao, S.-J. Lee, S. Nuryyeva, C. Zhu, K. Huynh, M. S. Goorsky, Y. Huang, X. Pan and Y. Yang, Solid-phase hetero epitaxial growth of α-phase formamidinium perovskite, *Nat. Commun.*, 2020, **11**, 5514.
32 Y. Numata, N. Shibayama and T. Miyasaka, $FAPbBr_3$ perovskite solar cells with V_{OC} values over 1.5 V by controlled crystal growth using tetramethylenesulfoxide, *J. Mater. Chem. A*, 2022, **10**, 672–681.
33 A. A. Sutanto, V. I. E. Queloz, I. Garcia-Benito, K. Laasonen, B. Smit, M. K. Nazeeruddin, O. A. Syzgantseva and G. Grancini, Pushing the limit of Cs incorporation into $FAPbBr_3$ perovskite to enhance solar cells performances, *APL Mater.*, 2019, **7**, 041110.
34 Y. Zhang, Y. Liang, Y. Wang, F. Guo, L. Sun and D. Xu, Planar $FAPbBr_3$ Solar Cells with Power Conversion Efficiency above 10%, *ACS Energy Lett.*, 2018, **3**, 1808–1814.
35 L. Zheng, M. Wei, F. T. Eickemeyer, J. Gao, B. Huang, U. Gunes, P. Schouwink, D. W. Bi, V. Carnevali, M. Mensi, F. Biasoni, Y. Zhang, L. Agosta, V. Slama, N. Lempesis, M. A. Hope, S. M. Zakeeruddin, L. Emsley, U. Rothlisberger, L. Pfeifer, Y. Xuan and M. Grätzel, Strain-induced rubidium incorporation into wide-bandgap perovskites reduces photovoltage loss, *Science*, 2025, **388**, 88–95.
36 C. Zhu, X. Niu, Y. Fu, N. Li, C. Hu, Y. Chen, X. He, G. Na, P. Liu, H. Zai, Y. Ge, Y. Lu, X. Ke, Y. Bai, S. Yang, P. Chen, Y. Li, M. Sui, L. Zhang, H. Zhou and Q. Chen, Strain engineering in perovskite solar cells and its impacts on carrier dynamics, *Nat. Commun.*, 2019, **10**, 815.
37 G. Kim, H. Min, K. S. Lee, D. Y. Lee, S. M. Yoon and S. I. Seok, Impact of strain relaxation on performance of α-formamidinium lead iodide perovskite solar cells, *Science*, 2020, **370**, 108–122.
38 H. Chen, C. Liu, J. Xu, A. Maxwell, W. Zhou, Y. Yang, Q. Zhou, A. S. R. Bati, H. Wan, Z. Wang, L. Zeng, J. Wang, P. Serles, Y. Liu, S. Teale, Y. Liu, M. I. Saidaminov, M. Li, N. Rolston, S. Hoogland, T. Filleter, M. G. Kanatzidis, B. Chen, Z. Ning and E. H. Sargent, Improved charge extraction in inverted perovskite solar cells with dual-site-binding ligands, *Science*, 2024, **384**, 189–193.
39 H. Wang, C. Zhu, L. Liu, S. Ma, P. Liu, J. Wu, C. Shi, Q. Du, Y. Hao, S. Xiang, H. Chen, P. Chen, Y. Bai, H. Zhou, Y. Li and Q. Chen, Interfacial Residual Stress Relaxation in Perovskite Solar Cells with Improved Stability, *Adv. Mater.*, 2019, **31**, 1904408.
40 J. Zhao, Y. Deng, H. Wei, X. Zheng, Z. Yu, Y. Shao, J. E. Shield and J. Huang, Strained hybrid perovskite thin films and their impact on the intrinsic stability of perovskite solar cell, *Sci. Adv.*, 2017, **3**, eaao5616.
41 S. Jung, Y. Choi, Y. Kim, Y. Jang, H. Jung, H. Jeon, J. Kim, E. Son, S. Jeong, J. M. Baik, J.-Y. Kim, J. Lu and H. Park, Strain engineering in vapor-deposited perovskites enables self-healing and stable solar cells, *Nano Energy*, 2025, **145**, 111482.
42 H. Yang, Z. Guo, Z. Xu, W. Cai, S. M. H. Qaid and Z. Zang, Crystallization Modulation Through Electron Transport Layer Surface Reconstruction Enables High-Performance Full-Air-Processed Perovskite Solar Cells, *Adv. Mater.*, 2025, **37**, e10967.
43 Q. Du, S. Feng, Y. Liang, B. Yu, J. Liu, Y. Li, W. Hong, L. Wang, G. Xing, J. Chen and D. Ma, Collaborative passivation of defects and enhancing crystallization enabled by an additive with multiple active sites for inverted perovskite solar cells, *Chem. Eng. J.*, 2025, **521**, 166733.
44 S. Tao, I. Schmidt, G. Brocks, J. Jiang, I. Tranca, K. Meerholz and S. Olthof, Absolute energy level positions in tin- and lead-based halide perovskites, *Nat. Commun.*, 2019, **10**, 2560.
45 C. Gong, H. Li, Z. Xu, Y. Li, H. Wang, Q. Zhuang, A. Wang, Z. Li, Z. Guo, C. Zhang, B. Wang, X. Li and Z. Zang, Efficient and stable inverted perovskite solar cells enabled by homogenized PCBM with enhanced electron transport, *Nat. Commun.*, 2024, **15**, 9154.
46 Y. Cai, J. Cui, M. Chen, M. Zhang, Y. Han, F. Qian, H. Zhao, S. Yang, Z. Yang, H. Bian, T. Wang, K. Guo, M. Cai, S. Dai, Z. Liu and S. (Frank) Liu, Multifunctional Enhancement for Highly Stable and Efficient Perovskite Solar Cells, *Adv. Funct. Mater.*, 2021, **31**, 2005776.
47 Y. Wang, L. Li, Z. Wu, R. Zhang, J. Hong, J. Zhang, H. Rao, Z. Pan and X. Zhong, Self-Driven Prenucleation-Induced Perovskite Crystallization Enables Efficient Perovskite Solar Cells, *Angew. Chem., Int. Ed.*, 2023, **62**, e202302342.
48 S. B. Shivarudraiah, N. Tewari, M. Ng, C.-H. A. Li, D. Chen and J. E. Halpert, Optically Clear Films of Formamidinium Lead Bromide Perovskite for Wide-Band-Gap, Solution-Processed, Semitransparent Solar Cells, *ACS Appl. Mater. Interfaces*, 2021, **13**, 37223–37230.
49 S. Li, C. Deng, L. Tao, Z. Lu, W. Zhang and W. Song, Crystallization Control and Defect Passivation via a Cross-Linking Additive for High-Performance $FAPbBr_3$ Perovskite Solar Cells, *J. Phys. Chem. C*, 2021, **125**, 12551–12559.
50 Q. Li, Y. Zheng, X. Guo, G. Zhang, G. Ding, Y. Shi, F. Li, M. Sun and Y. Shao, Interface Engineering Enhances the Photovoltaic Performance of Wide Bandgap $FAPbBr_3$ Perovskite for Application in Low-Light Environments, *Adv. Funct. Mater.*, 2023, **33**, 2303729.
51 A. S. Subbiah, N. Mahuli, S. Agarwal, M. F. A. M. van Hest and S. K. Sarkar, Towards All-Inorganic Transport Layers for

Wide-Band-Gap Formamidinium Lead Bromide-Based Planar Photovoltaics, *Energy Tech.*, 2017, **5**, 1800–1806.

52 A. S. Subbiah, S. Agarwal, N. Mahuli, P. Nair, M. Van Hest and S. K. Sarkar, Stable p–i–n $FAPbBr_3$ Devices with Improved Efficiency Using Sputtered ZnO as Electron Transport Layer, *Adv. Mater. Interfaces*, 2017, **4**, 1601143.

53 A. Dolgormaa, Y. Wu, Z. Xu, H. Zhu, Y. Zhang, S. Lian, W. Wu, B. Li, H. Zhan, L. Wang and C. Qin, High-Efficiency and Stable $FAPbBr_3$ Perovskite Solar Cells Enabled by 3,7-POPA: A Multifunctional Phenoxazine-Based Self-Assembled Monolayers, *Adv. Funct. Mater.*, 2026, **36**, e16065.

